Structural, optical and electrical properties of NiMO4 (M=W and Mo)

Marwa Krichen, Nidhal Drissi, Karim Karoui, Fathi Jomni

Structural, optical and electrical properties of $NiMO_4$ (M=W and Mo)

Marwa krichen[a], Nidhal Drissi[b], Karim Karoui[a,c*] and Fathi Jomni[d]

[a] Laboratory LaSCOM, University of Sfax, BP1171, 3000, Sfax, Tunisia

[b] Department of physics, Faculty of Science, king Khalid University, P.O. Box 9004, Abha 61413, Saudi Arabia

[c] GREMAN UMR 7347-CNRS, CEA, INSACVL, University of Tours, Blois, France

[d] Université de Tunis El Manar, Laboratoire LMOP, LR99ES17, El Manar, 2092 Tunis, Tunisia

*Corresponding author: karouikarim36@yahoo.com

Abstract

The $NiMO_4$ (M=Mo and W) samples have been synthesized with solid-state reaction method at high temperature. The structural, optical, and electrical transport properties were investigated. X-ray diffraction data refined via Rietveld method showed the monoclinic system for these compounds. The UV/Vis optical spectra indicates that the direct gap energy values are 2.72 eV for $NiMoO_4$ and 2.81 eV for $NiWO_4$ compounds which can be promising candidates for semiconductors applications. These materials were characterized by impedance spectroscopy technique measured in the $1 - 10^6$ Hz frequency and 398 - 533K temperatures range. The AC conductivity was analyzed using the Jonscher power law, which showed that the conduction mechanisms are well described by the non-overlapping small polaron-tunneling model (NSPT) in phase I and the correlated barrier-hopping model (CBH) in phases II for the Mo-based compound. Moreover, the overlapping-large polaron tunneling (OLPT) model for $NiWO_4$ compound. The conduction mechanism was interpreted with the help of Elliot's theory, and the Elliot's parameters were determined. The comparative study of the two titled compounds shows better properties for the Mo-based compounds.

Keyword: *Crystal structure, Phase transition, Optic, Electric properties, conduction mechanism.*

Introduction

The tungsten (W) and molybdenum (Mo) involved in materials such as oxides, nitrides, and oxysalts also have received much attention, due to their remarkable record of widespread applications in various fields of materials science, such as photocatalysis, phosphors, light-

emitting diodes, optical fibers, humidity sensors, scintillators, and magnetic properties[1]. Moreover, they have been proven to be feasible for electrochemical energy storage due to their high specific capacity, low working voltage, abundant reserves, and environmental friendliness [2-5]. Among them, cobalt tungstate ($CoWO_4$) and nickel tungstate ($NiWO_4$) have been researched as promising replacements for catalysis[6], dielectric ceramics[7], oxygen-evolving electro-catalysts[8], and supercapacitors [9-11]. The crystalline structures of materials based on tungstates or molybdates are of the scheelite type with the tetragonal space group or of the wolframite type with the monoclinic space group. For the scheelite structure, each tungsten atom is surrounded by four oxygen atoms, whereas in the wolframite structure, every tungsten is surrounded by six oxygen atoms[12]. Also, the use of molybdenum instead of tungsten can influence the type of structure and consequently the optical and electrical properties. In this context, in the present work, we report on the correlation among the structural, optical, and electrical properties of the $NiMoO_4$ and $NiWO_4$ materials and the effect of substitution tungsten with molybdenum on the optical and electrical properties.

Experimental section

Mixed stoichiometric amounts NiO, MoO_3 and WO_3 were used to synthesize the $NiMoO_4$ and $NiWO_4$ compounds via conventional solid state reaction method. The starting reagents were mixed and ground thoroughly in an agate mortar. They were heated to 550 °C for 60 h to release oxygen gas. The resulting powders were pressed into cylindrical pellets and heated at 850 °C for 160 h.

Results and Discussions

1- X-ray diffraction analysis

The Structural refinement was carried out for the studied compound $NiMO_4$ (M=Mo and W) using Rietveld's refinement program «Full Proof». The pseudo-Voigt peak profile function was used, and the background was approximated by linear interpolation between a set of background points with refinable heights.

X-ray diffraction patterns of the synthesized compounds are shown in **Fig. 1 (a) and (b)**, respectively. The small difference between the calculated/experimental patterns and the low values of the agreement parameters confirms the successful refinement of the experimental data. The powder pattern of $NiMoO_4$ indicates that it's isostructural with the $CoMoO_4$ structure [14] where is indexed based on a monoclinic system with the C2/m space group and the cell

parameters: a=9.5111 Å, b=8.7601 Å, c=7.6673 Å, β=113.11°, V=587.56 Å^3 and Z=8 with a reliability factor of χ^2=4.93. The $NiWO_4$ is isostructural with the $MgWO_4$ [15] where is indexed on a monoclinic system with the P 2/c space group. The corresponding cell parameters obtained from the data are as follows: a=4.6013 Å, b=5.6632 Å, c=4.9103 Å, β=90.03°, V=127.95 Å^3 and Z=4 with a reliability factor of χ^2=1.05. The refined structural parameters of $NiMoO_4$ and $NiWO_4$ are summarized in **Table 1**

[16-17]. The structures of studied compounds are presented in **Fig. 2(a)** and **Fig.2(b)** for $NiMoO_4$ and $NiWO_4$ respectively.

For $NiMoO_4$, projected on the (101) plane, the Ni and Mo ions occupy two different crystallographic sites, while for the tungstate compound, Ni and W ions occupy a single site which can be explain the difference in the volume. Rietveld refinement allows us to determine atomic positions for each studied compound and illustrated in **Table 2**. Interatomic distances are reported in **Table 3** for both studied compounds.

The wolframite structure of these samples found that both Ni and M (M=Mo and W) atoms are surrounded by six oxygen atoms, forming distorted octahedral. These later, NiO_6 and MO_6 octahedral, share edges and form zigzag chains along the C axis for $NiWO_4$ (**Fig. 2(b)**). In particular, the WO_6 (MoO_6) octahedral are highly distorted since two of the W-O distances are much larger than the other four distances. Thes presence of three bonding pairs Ni-O and M-O with different lengths is due to the two types of non-equivalent oxygen atoms. This result can be affecting the electrical and optical properties.

2- Gap energy

To know the potential application of these materials in the optoelectronic field, we investigated the optical properties of $NiWO_4$ and $NiMoO_4$. **Fig. 3 (a, b)** displays the UV/vis absorption spectra at room temperature of $NiWO_4$ and $NiMoO_4$, respectively in 200–800 nm wavelength range. Both compounds exhibit good light absorption properties in UV and visible regions. The intense absorption peak at 350nm may be attributed to charge transfer in the WO_6/ or MoO_6 matrix, while the other peaks in the visible region are due to the forbidden electronic transition from $^3A_{2g}$ to ^1E_g and the electronic transition from $^3A_{2g}$ to ^1T_g, respectively[18]. The type of band gap is highly related to the optical absorption characteristics. The absorption spectra of these compounds display peaks in the ultraviolet spectral region, suggesting a direct band gap [19-23]. Based on the Tauc's relation [24], we calculated the direct gap energy by the extrapolation the linear part of the curve to the energy axis as shown in the inset of Fig. 3. The direct gap energy values are 2.72 eV for $NiMoO_4$ and 2.81eV for $NiWO_4$. This slight difference may be due to

differences in Mo-O and W-O distances in the MoO_6 and WO_6 octahedral, where they are smaller for the Mo-based compound. These values of E_g indicate the semiconductor character of the synthesized samples and their potential for optoelectronic applications [25].

3- Nyquist diagrams and grain conductivity

This technique analyzes the ac response of a system, separates the real and imaginary components of the electrical parameters, and provides a true picture of the material properties. When impedance data of materials that have capacitive and resistive components are represented in the Nyquist plot, they appear in the form of a succession of semicircle representing electrical phenomena due to bulk material, grain boundary effect and interfacial phenomena [26-27].

The Nyquist plots of $NiMoO_4$ and $NiWO_4$ at different temperatures are shown in **Fig. 4 (a, b)** respectively. For the Mo-based compound, as shown in **Fig. 4 (a)**, the Nyquist plot shows two semicircular arcs correspond to the grain and gran boundary response. The centers of semicircles that compose the total electric response are centered below of real axis (Z′) which confirms the presence of non-Debye type of relaxation in the materials. These diagrams were successfully modeled by an equivalent circuit model (**inset Fig. 4 (a)**) which described the electrical behavior of these materials.

For the W-based compound, the Nyquist plot is shown in **Fig. 4 (b)** which exhibits a single semicircular arc. The absence of second semicircle in the complex impedance plots suggests the dominance of bulk contributions. The impedance components were fitted to an equivalent circuit, which consist of a parallel combination of resistance R1, capacitance C1, and fractal capacity CPE1[28]. To justify the choice of equivalent circuit, we present in **Fig. 4 (b)** the experimental and simulated impedance spectra at different temperature in Cole–Cole representation. For both studied compounds, we note that as the temperature increases, the radius of the arc corresponding to the bulk resistance of the sample decreases, indicating an activated thermal conduction mechanism and proved the semiconductor character of these materials.

Relying on the grain resistance values obtained by modeling curves by the equivalent circuit and the sample dimensions, the conductivity of the grain (σ_g) can be calculated using the relationship:

$$\sigma_g = \frac{e}{R_1 S} \qquad (1)$$

where S is the electrolyte-electrode contact area and e is the thickness of the sample.

The electrical conductivity σ_g increases with increasing temperature, indicating an Arrhenius-type behavior [29]. To understand the conduction phenomena and calculate the activation energies we plot in the following **Fig. 5 (a)** and **Fig. 5 (b)** the thermal evolution of the specific conductivity [Ln(σ_g) vs. 1000/T], for $NiMoO_4$ and $NiWO_4$ respectively.

A change in the slope curve around 450K for the Mo-based compound is observed which. can be explained by the change in the conduction mechanism in this material.

Based on linear fitting, the activation energy values for the $NiMoO_4$ sample are equal to E_{aI} =0.12 eV and E_{aII} = 0.17 eV at lower and higher temperatures, respectively. The activation energy obtained for the tungstate compound, is greater than that obtained for Mo-based compound, at about Ea=0.6 eV. These results indicate better electrical properties for the Mo-based compound which is consistent with the obtained optical results.

Furthermore, the difference in activation energy of the titled compound can be explained by the difference in structure and volume where the charge carriers in the Mo-based material have more room to move.

4- AC electrical conductivity

4-1. Temperature and frequency dependence of AC conductivity

The ac conductivity σ_{ac} is determined from experimental data of the real and imaginary part of the complex impedance Z* as follows:

$$\sigma_{ac}(\omega, T) = \frac{e}{s} \frac{Z'}{(Z'^2 + Z''^2)} \qquad (2)$$

The frequency-dependent AC conductivity plots at various temperatures are presented in **Fig.6 (a)** and **Fig. 6 (b)** for $NiMoO_4$ and $NiWO_4$, respectively.

It is observed that, for both studied compounds, the conductivity exhibits a dispersion pattern at high frequencies, which shifts towards higher frequencies with increasing temperature, attributed to the ac conductivity and characterized by ω^s. However, the plateau region at low frequencies corresponds to the dc conductivity of the material.

To analyze, the spectra, they were fitted using the expression proposed by Jonsher [30]:

$$\sigma_{ac} = \sigma_{dc} + A\,\omega^s \qquad (3)$$

where A is a constant that depends on temperature and determines the strength of polarization and (s) is an exponent that is less than or equal to unity and represents the degree of interaction between mobile ions and their surrounding lattices.

According to Funke [31], if s <1, it would indicate that the hopping process involves a translational motion with a big hop of charge carriers. Whereas, if s > 1, we deduce that the motion involved is a localized hopping of the species with a small hop without leaving the neighborhood.

The temperature dependence of the dc conductivity plotted against the temperature in an Arrhenius plot is shown in **Fig. 7 (a)** and **Fig. 7 (b)** for molybdate and tungsten compounds respectively. For $NiMoO_4$ (**Fig. 7 (a))** the variation of the dc conductivity with absolute temperature shows two regions associated with two activation energies separated by a temperature of T= 450K (E_{dc}(I)=0.1 eV and E_{dc}(II)=0.17 eV corresponding respectively to lower and higher temperature phases). Whereas dc conductivity of $NiWO_4$ shows a linear variation with the activation energy is E_{dc}=0.46 eV (**Fig. 7 (b)**). This single valued activation energy suggests that the conduction phenomenon of the compound over the measured temperature range is described by a single mechanism.

The obtained value presents better conduction for the molybdate compound, which can be explained by the difference in crystal structures of the titled compounds. The conduction phenomenon of $NiMO_4$ (M=Mo and W) occurs through hopping of ions. the electron transfers from one Ni^{2+} ion to the adjacent Ni^{2+} ion, leading to the formation of Ni^{3+} ion [32]:

$$Ni^{2+} \leftrightarrow Ni^{3+} + e^{-}$$

The difference between the values of activation energy obtained by impedance spectroscopy and ac conductivity confirms that the transport in $NiMO_4$ (M=Mo and W) is not due to a simple hopping mechanism.

To determine the predominant conduction mechanism of the AC conductivity of the investigated compounds, the variation of the exponent "s" as a function of temperature is an adequate method to gain more insight into the origin of the conductivity from the conduction models[33]. For the Mo-based compound (**Fig. 8 (a)**) the frequency exponent s exhibits two distinct regions as follows: region I in which the value of s increase with the increase of temperature that corresponds to the NSPT model, and it decreases in region II with the increase of temperature corresponding to the CBH model. This change of the conduction model is the origin of the change of activation energy in the conductivity variation of the Mo based compound. Moreover, for the tungstate compound presented in **Fig. 8 (b)**, it seems that the conduction is associated with the OLPT model where s decreases with increasing temperature to a minimum value at a certain temperature, and then continues to increase with increasing temperature.

4-2. Theoretical investigation of non-overlapping small polaron tunneling (NSPT) conduction mechanism of $NiMoO_4$ (region I):

In the region I of $NiMoO_4$ (T≤470K) the NSPT seems to be the most appropriate model describes this phase. According to the tunneling model, the frequency exponent (s) is given by the equation[34]:

$$s = 1 - \frac{4}{Ln\left(\frac{1}{\omega\tau_0}\right) - \frac{W_H}{T}} \quad (4)$$

where W_H is the polaron hopping energy, k_B the Boltzmann constant and τ_0 is a characteristic relaxation time of the order of $\tau_0 = 10^{-13}$ s.

In this model, the AC conductivity is given by:

$$\sigma(\omega) = (\pi e)^2 kT\alpha^{-1}\omega[N(E_F(T))]^2 \frac{R_\omega^4}{12} \quad (5)$$

with $$R_\omega = \frac{1}{2\alpha}\left[Ln\left(\frac{1}{\omega\tau_0}\right) - \frac{W_H}{kT}\right] \quad (6)$$

In the above equations, α^{-1} is the spatial extension of the polaron (= 1×10^{10} m), N (E_F) is the density of states at the Fermi level, R_ω is the tunneling distance and W_H represents the polaron hopping energy.

The variation of (Ln(σ_{ac})) as a function of temperature at different frequencies is given in **Fig. 9**, As we can see, the theoretical curves (lines) are in good agreement with the experimental results (symbols).

The value of N(E_F) and α^{-1} obtained by fitting are reasonable for localized states. Moreover, the plot of the variations of the state density N (E_F) versus frequency is shown in **Fig. 10**.

These parameters increase with frequency, which is in good agreement with the literature[35]. The reasonably high values of the density of states N (EF) (~10^{15} eV^{-1} cm^{-1}) imply that the hopping between pairs of sites overpowers the mechanism of charge transport in this compound.

The variation of the tunneling distance R_ω, calculated from **Eq. 6**, as a function of temperature is illustrated in **Fig. 10 (inset)**. We observe a decrease in the value of R_ω as the frequency increases. The value of R_ω is about the interatomic distance which is in good agreement with the results predicted by Eliott[36].

4-3. Theoretical investigation of the correlated barrier hopping (CBH) conduction mechanism of $NiMoO_4$ (region II):

Fig. 8 (a) shows the values of s where is decrease with increasing temperature for NiMoO4 (region II). In this model (CBH), the conduction occurs via single polaron (or bipolaron)

hopping process over the Coulomb barrier separating two defect centers. The binding energy has been computed from the following relation [37]:

$$S = 1 - \frac{6K_BT}{W_M - K_BTLn(\omega\tau_0)} \qquad (7)$$

The value of W_M can be calculated from the previous equation by plotting (1-s) versus temperature as shown in the inset of **Fig. 8 (a)**.

According to CBH model, the ac conductivity is given by[38]:

$$\sigma_{ac} = \frac{n}{24}\pi^2\omega NN_p\varepsilon' R_\omega^6 \qquad (8)$$

where n is the number of polarons involved in the hopping process (n = 1 for single polaron and n = 2 for bipolaron processes), NN_p is proportional to the square of the concentration of states, and ε′ is the dielectric constant. The hopping distance for conduction (ωτ=1), R_ω is given as:

$$R_\omega = \frac{4ne^2}{\pi\varepsilon_0\varepsilon'[W_M - K_BTLn(1/\omega\tau_0)]} \qquad (9)$$

As shown in the inset **Fig. 8 (a)**, the fit of the curve in region II allows us to determine the value of potential barrier W_M which was found to be 0.04eV.

The obtained W_M value is approximately a quarter of the activation energies ($W_M=E_a/4$), which suggests that single polaron hopping is the dominating conduction mechanism in $NiMoO_4$ compound.

Fig. 11 displays the temperature dependence of AC conductivity ($Ln(\sigma_{ac})$) in region II. It is obvious that the AC conductivity varies exponentially with temperature and the curves are straight lines. The values of N and W_M are listed in **Table 4** where we can deduce that an increase in the frequency causes a decrease in the localized states density. Depending on the definition agreed by Mott [39] we can attribute the reduction of the localized states density as a function of the frequency to the increase in the disorder, leading to a decrease in the stabilities of states from which the non-localization of the latter can occur.

The variation of R_ω as a function of the frequency in region II for the molybdate compound is shown in **Fig. 12**.

The hopping distance (R_ω) decreases as the frequency increases. This behavior agrees with the increment of the parameter N as the frequency increases (**Table 4**). It is noteworthy that when the density of localized states (N) and the conductivity increase with the frequency, the barrier height W_M decreases slightly. Consequently, the charges can jump readily at the nearest neighbor sites.

4-4. Theoretical analysis of the overlapping large Polaron tunneling (OLPT) conduction mechanism of $NiWO_4$

Figure 8 (b) shows the exponent (s) plotted as a function of temperature which is decreases and exhibits a minimum at a certain temperature before starting to increase with temperature indicating that the conduction mechanism in $NiWO_4$ is more likely explained by the OLPT model[40]:

$$\sigma_{ac} = \frac{\pi^4 e^2 K_B^2 T^2 \alpha^{-1}\, \omega\, [N(E_F)]^2\, R_\omega^4}{12(2\alpha K_B T + \frac{W_{H0} r_p}{R_\omega^2})} \qquad \textbf{(10)}$$

where r_p is large polaron radius, α is inverse localization length, $N(E_F)$ is the density of states at the Fermi level, K_B is Boltzmann constant, W_{H0} is the activation energy associated with charge transfer between the overlapping sites and R_ω is the hopping length at angular frequency ω (is the tunneling distance). The hopping length R_ω is determined in this model by solving the following quadratic equation:

$$(R'_\omega)^2 + \left(\beta W_{H0} + Ln(\omega\tau_0)\right)R'_\omega - \beta W_{H0} r'_p = 0 \qquad \textbf{(11)}$$

$$R_\omega' = 2\alpha R_\omega,\ r_p' = 2\alpha r_p \text{ and } \beta = 1/k_B T \qquad \textbf{(12)}$$

where W_H is the polaron hopping energy, R is the polaron jump distance, and r_p is the polaron radius. The parameters W_{H0} and R_ω can be calculated using the following relations:

$$W_{H0} = \frac{e^2}{4\varepsilon_p r_p} \qquad \textbf{(13)}$$

$$R_\omega = \frac{1}{4\alpha}\left\{\left(Ln\left(1/\omega\tau_0\right) - W_{H0}\beta\right) + \left[\left(W_{H0}\beta - Ln\left(1/\omega\tau_0\right)\right)^2 + 8\alpha W_{H0} r_p \beta\right]^{1/2}\right\} \qquad \textbf{(14)}$$

and the frequency exponent s in the overlapping large polaron tunneling model was given by [36]:

$$S = 1 - \frac{8\alpha R_\omega + \frac{6 W_{H0} r_p}{R_\omega r_p T}}{[2\alpha R_\omega + \frac{W_{H0} r_p}{R_\omega K_B T}]^2} \qquad \textbf{(15)}$$

The variation of the AC conductivity with temperature at different frequencies (**Fig. 13**.) shows the decrease conductivities with the temperature which is thermally activated. Furthermore, the OLPT model was used to obtain the best fits for these graphs, revealing that the simulated conductivities are in good agreement with the experimental data. The fitted parameters α, W_{H0} and r_p are summarized in **Table 5**.

Among the refinement results, the evolution of the density of states at the Fermi level $N(E_F)$ as a function of frequency is presented in **Fig. 14**. The shape of this variation shows that an increase in frequency stimulates the mobility of free charge, which may cause an increase in the radius of the polaron (r_p) and thus justify the increase in AC conductivity with frequency.

As shown in the inset Fig. **14**, the thermal variation of the tunneling distance R_ω for different frequencies shows that when the temperature increases, the tunneling distance R_ω increases, implying that the increase in temperature provides thermal energy to polarons, which subsequently move and facilitate hopping and interchain interaction. For a fixed temperature, R_ω decreases with frequency. The R_ω hopping distance deduced from the previous study is in the order of magnitude of the interatomic distance. These results suggest that the conduction process of the tungsten studied compound is ensured by the movement of the Ni^{2+} cation along the (100) tunnels direction.

Conclusions

In this study, we successfully synthesized the $NiMoO_4$ and $NiWO_4$ compound by using the solid-state method. X-ray diffraction analysis performed at room temperature revealed that the structure of both compounds is monoclinic. The UV-Vis spectroscopy was investigated to decide certain main parameters, such as, the direct gap energy values, which are 2.72 eV for $NiMoO_4$ and 2.81eV for $NiWO_4$ compounds. The Nyquist plots were analyzed using an equivalent circuit model for each studied compound. Furthermore, we interpreted the high frequency dependent AC conductivity of $NiMO_4$ (M=Mo and W) using the universal Jonscher's law. The temperature dependence of the exponent s reveals that the conduction mechanism is explained by the non-overlapping small polaron-tunneling model (NSPT) in phase I and the correlated barrier-hopping model (CBH) in phases II for Mo-based compound. While the overlapping large Polaron tunneling (OLPT) model was used for $NiWO_4$. Based on the optical and electrical results, the Mo- based compound exhibited better properties which can be explained by the differences in Mo-O and W-O distances in the MoO_6 and WO_6 octahedral where the Mo-based compound has smaller distances.

Conflicts of interest

There are no conflicts to declare.

Acknowledgment

The authors extend their appreciation to the Deanship of Scientific Research at King Khalid University for funding this work through small group Research Project under grand number RGP/41/44.

References

[1] Y. Li, S. Tan, J. Jiang, Z.Huang, X. Tan, Room-temperature synthesis, growth mechanism and properties of uniform $CdMoO_4$ nano-octahedra, Cryst.Eng.Comm 13 (2011) 2649–2655.

[2] Gong C, Bai YJ, Feng J, Tang R, Qi YX, Lun N, Fan RH., Enhanced Electrochemical Performance of $FeWO_4$ by Coating Nitrogen-Doped Carbon, ACS Appl Mater Interfaces 5 (2013) 4209–4215.

[3] Shim HW, Lim AH, Kim JC, Lee GH, Kim DW, Hydrothermal Realization of a Hierarchical, Flowerlike $MnWO_4$@MWCNTs Nanocomposite with Enhanced Reversible Li Storage as a New Anode Material, Chem Asian J 8 (2013) 2851–2858.

[4] Zhang E, Xing Z, Wang J, Ju ZC, Qian YT, Enhanced energy storage and rate performance induced by dense nanocavities inside $MnWO_4$ nanobars, RSC Adv 2 (2012) 6748–6751.

[5] Zhang LS, Wang ZT, Wang LZ, Xing Y, Li XF, Zhang Y, Electrochemical performance of $ZnWO_4$/CNTs composite as anode materials for lithium-ion battery, J Mater Sci 305 (2014) 179–185.

[6] Hitoki G, Takata T, Ikeda S, Hara M, Kondo JN, Kakihana M, Domen K, Mechano-catalytic overall water splitting on some mixed oxides, Catal Today, 63 (2000) 175–181.

[7] Pullar RC, Farrah S, Alford NM, $MgWO_4$, $ZnWO_4$, $NiWO_4$ and $CoWO_4$ microwave dielectric ceramics, J Eur Ceram Soc 27 (2007) 1059–1063.

[8] Srirapu VKVP, Kumar A, Srivastava P, Singh RN, Sinha ASK, Nanosized $CoWO_4$ and $NiWO_4$ as efficient oxygen-evolving electrocatalysts, Electrochim Acta 209 (2016) 75–84.

[9] Kumari N, Singh RN, Nanocomposites of nitrogen-doped graphene and cobalt tungsten oxide as efficient electrode materials for application in electrochemical devices, AIMS Mater Sci 3 (2016) 1456–1473.

[10] Xu, X. Y.; Gao, J. P.; Huang, G. B.; Qiu, H. X.; Wang, Z. Y.; Wu, J. Z.; Pan, Z.; Xing, F. B. Fabrication of $CoWO_4$ @$NiWO_4$ nanocomposites with good supercapacitve performances, Electrochim Acta, 174 (2015) 837–845.

[11] He GJ, Li JM, Li WY, Li B, Noor N, Xu K, Hu JQ, Parkin IP, one pot synthesis of nickel foam supported self-assembly of $NiWO_4$ and $CoWO_4$ nanostructures that act as high-performance electrochemical capacitor electrodes, J Mater Chem A 3 (2015) 14272– 14278.

[12] S. Rajagopal, D. Nataraj, O.Yu. Khyzhun, Y. Djaoued, J. Robichaud, D. Mangalaraj, Hydrothermal synthesis and electronic properties of $FeWO_4$ and $CoWO_4$ nanostructures, J. Alloys Compd. 493 (2010) 340–345.

[13] Yi Ding, Yong Wan, Yu-Lin Min, Wei Zhang, Shu-Hong Yu, General Synthesis and Phase Control of Metal Molybdate Hydrates $MMoO_4 \cdot nH_2O$ (M = Co, Ni, Mn, n = 0, 3/4, 1) Nano/Microcrystals by a Hydrothermal Approach: Magnetic, Photocatalytic, and Electrochemical Properties, Inorg. Chem. 47 (2008) 7813-7823.

[14] H. Ehrenberg , I. Svoboda, G. Wltschek, M. Wiesmann , F. Trouw, H. Weitzel, H. Fuess, Crystal and magnetic structure of α-$NiMoO_4$, Journal of Magnetism and Magnetic Materials 150 (1995) 371-376.

[15] Rolland O, Keeling JR, The structure of $NiWO_4$, Acta Cryst 10 (1975) 209-213.

[16] B Gassoumi, R Jaballah, A Boukhachem, N Kamoun-Turki, M Amlouk, Simple route deposition and some physical investigations on nanoflower $NiMoO_4$ sprayed thin films, Bull. Mater. Sci., 44 (2021) 128.

[17] Maria N. Mancheva, Reni S. Iordanova, Dimitar G. Klissurski, Georgi T. Tyuliev, Boris N. Kunev, Direct Mechanochemical Synthesis of Nanocrystalline $NiWO_4$, J. Phys. Chem. C 111 (2007) 1101-1104.

[18] A. L. M. de Oliveira, J. M. Ferreira, Marcia R. S. Silva, Soraia C. de Souza, F. T. G. Vieira, E. Longo, A. G. Souza, Ieda M. G. Santos, Influence of the thermal treatment in the crystallization of $NiWO_4$ and $ZnWO_4$, J Therm Anal Calorim 97 (2009) 167–172.

[19] Dohner ER, Hoke ET, Karunadasa HI, Self-assembly of broadband white light emitters , J Am Chem Soc 136 (2014) 1718–1721.

[20] Hu T, Smith MD, Dohner ER, Sher M-J, Wu X, Trinh MT, Fisher A, Corbett J, Zhu X-Y, Karunadasa HI, Lindenberg AM, Mechanism for Broadband White-Light Emission from Two-Dimensional (110) Hybrid Perovskites, J Phys Chem Lett 7 (2016) 2258–2263.

[21] Ramanaa CV, Carbajal-Franco G, Vemuri RS, Troitskaia IB, Gromilov SA, Atuchin VV, Optical properties and thermal stability of germanium oxide (GeO_2) nanocrystals with α-quartz structure, Mater Sci Eng B 174 (2010) 279–284.

[22] Atuchin VV, Isaenko LI, Kesler VG, Kang L, Lin Z, Molokeev MS,Yelisseyev AP, Zhurkov SA, Structural, Spectroscopic, and Electronic Properties of Cubic G0-Rb_2KTiOF_5 Oxyfluoride, J Phys Chem C 117 (2013) 7269–7278.

[23] Ma L, Xia Z, Atuchin V, Molokeev M, Auluck S, Reshak AH, Liu Q, Engineering oxygen vacancies towards self-activated $BaLuAl_xZn_{4-x}O_{7-(1-x)/2}$ photoluminescent materials: an experimental and theoretical analysis, Phys Chem Chem Phys 17 (2015) 31188–31194.

[24] Ross-Medgaarden EI, Wachs IE, Structural Determination of Bulk and Surface Tungsten Oxides with UV−vis Diffuse Reflectance Spectroscopy and Raman Spectroscopy, J Phys Chem C 111 (2007) 15089–15099.

[25] Li H-J, Liu Y-L, Chen X-G, Gao J-X,Wang Z-X, LiaoW-Q, High-Temperature Dielectric Switching and Photoluminescence in a Corrugated Lead Bromide Layer Hybrid Perovskite Semiconductor, Inorg Chem 58 (2019) 10357–10363.

[26] R.G.M. Oliveira M.C. Romeu, M.M. Costa, P.M.O Silva, J.M.S. Filho,C.C.M. Junqueira, A.S.B. Sombra, Impedance spectroscopy study of $Na_2Nb_4O_{11}$ ceramic matrix by the addition of Bi_2O_3, Journal of Alloys and Compounds 584 (2014) 295–302.

[27]Prasanta Dhak, Debasis Dhak, Manasmita Das, Kausikisankar Pramanik, Panchanan Pramanik, Impedance spectroscopy study of $LaMnO_3$ modified $BaTiO_3$ ceramics , Materials Science and Engineering B 164 (2009) 165–171.

[28] Shukdev Pandey, Devendra Kumar, Om Parkash, Lakshman Pandey Equivalent circuit models using CPE for impedance spectroscopy of electronic ceramics, Integrated Ferroelectrics183 (2017) 141-162.

[29] Changlong Li , Yufei Liu, Jian He, Kyle S. Brinkman, Ga-substituted $Li_7La_3Zr_2O_{12}$: An investigation based on grain coarsening in garnet-type lithium ion conductors, Journal of Alloys and Compounds 695 (2017) 3744-3752.

[30] Manel ben Abdessalem, Abdelhedi Aydi, Najmeddine Abdelmoula, Raman scattering, structural, electrical studies and conduction mechanism of $Ba_{0.9}Ca_{0.1}Ti_{0.95}Zr_{0.05}O_3$ ceramic, Journal of Alloys and Compounds 774 (2019) 685-693.

[31] K. Funke, Jump relaxation in solid electrolytes, Progress in Solid State Chem. 22 (1993) 111-195.

[32] Ying Liu, Pu Liu, Wei Qin, Xiaoju Wu, Guowei Yang, Laser modification-induced $NiCo_2O_{4-\delta}$ with high exterior Ni^{3+}/Ni^{2+} ratio and substantial oxygen vacancies for electrocatalysis, Electrochimica Acta 297 (2019) 623-632.

[33] L. Essaleh, S. Amhil, S.M. Wasim, G. Marín, E. Choukri, L. Hajji, Theoretical and experimental study of AC electrical conduction mechanism in the low temperature range of p-$CuIn_3Se_5$, Physica E: Low-dimensional Systems and Nanostructures 99 (2018) 37–42.

[34] Marwa Enneffati, Bassem Louati, Kamel Guidara, Synthesis, refinement of the structure, and AC conductivity behavior of sodium lithium orthonavadates, Ionics 23 (2017) 1115–1129.

[35] S. Nasri, M. Megdiche, M. Gargouri, DC conductivity and study of AC electrical conduction mechanisms by non-overlapping small polaron tunneling model in $LiFeP_2O_7$ ceramic, Ceramics International 42 (2016) 943-951.

[36] S.R. Elliott, Ac conduction in amorphous chalcogenide and pnictide semiconductors, Adv. Phys. 36 (1987) 135–217.

[37] Y. Ben Taher, A. Oueslati, N. K. Maaloul, K. Khirouni, M. Gargouri, Conductivity study and correlated barrier hopping (CBH) conduction mechanism in diphosphate compound , Applied Physics A 120 (2015) 1537–1543.

[38] Sourour Ben Yahya, Regis Barillé, Bassem Louati, Synthesis, optical and ionic conductivity studies of a lithium cobalt germanate compound, RSC Adv. 12 (2022) 6602–6614.

[39] N. F. Mott, E. A. Davis, Disordered Materials: Electronic Processes in Non-Crystalline Materials., Sec. Ed. Clarendon Press, Oxford (1979).

[40] Sahel Karoui, Slaheddine Kamoun, Study of dielectric relaxation and polaron conductivity mechanism in sodium nitroprusside (SNP): $Na_2[Fe(CN)_5(NO)]\cdot 2H_2O$, Physica E 132 (2021) 114771.

Figures caption

Fig. 1 (a, b): Refined powder X-ray diffraction pattern for **(a)** $NiMoO_4$ and **(b)** $NiWO_4$, at room temperature: calculated data (black solid line), observed data (red)and the Bragg positions are observable by vertical bar.

Fig. 2 (a, b): The crystal structure of **(a)** $NiMoO_4$ and **(b)** $NiWO_4$

Fig. 3 (a, b): The UV/vis absorption spectra at room temperature of **(a)** $NiMoO_4$ and **(b)** $NiWO_4$ compounds.

Fig. 4 (a, b): Complex impedance spectra at various temperatures of **(a)** $NiMoO_4$ and **(b)** $NiWO_4$ with electrical equivalent circuit **(inset)**.

Fig. 5 (a, b): Variation of the Ln (σ_g) as function of temperature of **(a)** Mo and **(b)** W based compound.

Fig. 6(a, b): Frequency dependence of alternating current conductivity at several temperatures for **(a)** $NiMoO_4$ and **(b)** $NiWO_4$.

Fig. 7(a, b): Variation of the Ln (σ_{dc}) as function of temperature of **(a)** $NiMoO_4$ and **(b)** $NiWO_4$.

Fig. 8 (a, b): Variation for universal exponent s as a function of Temperature for **(a)** $NiMoO_4$ and **(b)** $NiWO_4$

Fig. 9: Comparative analysis of theoretical and experimental ac conductivity for $NiMoO_4$ (region I) at different frequencies.

Fig. 10: Variation of the parameter N (eV^{-1} cm^{-1}) according to the frequency (NSPT model) and the variation of the tunneling distance R_ω (Å) as a function of temperature at different frequencies of $NiMoO_4$ (NSPT model) **(inset)**

Fig. 11: Variation of Ln (σ_{ac}) with inverse of temperature at various frequencies for $NiMoO_4$ (CBH model)

Fig. 12: Variation of the hopping tunneling distance R_ω as a function as temperature at different frequencies (CBH model)

Fig. 13: OLPT model fitting of ac conductivity at different frequency values for $NiWO_4$ compound.

Fig. 14: Variation of the parameters $N(E_F)$ (eV^{-1} cm^{-3}) according to the frequency (OLPT model) and temperature dependence of the tunneling distance R_ω(Å) at different frequencies for $NiWO_4$ (OLPT model) **(inset)**

Tables caption:

Table 1: Crystal data of the $NiMoO_4$ and $NiWO_4$ compounds.

Table 2: Fractional atom coordinates for $NiMO_4$ with M=Mo and W from X-ray powder diffraction data.

Table 3: Comparison of polyhedral and interatomic distances of $NiMoO_4$ and $NiWO_4$ compound.

Table 4: Parameters used for CBH model fitting in $NiMoO_4$

Table 5: Parameters used for OLPT model fitting in $NiWO_4$

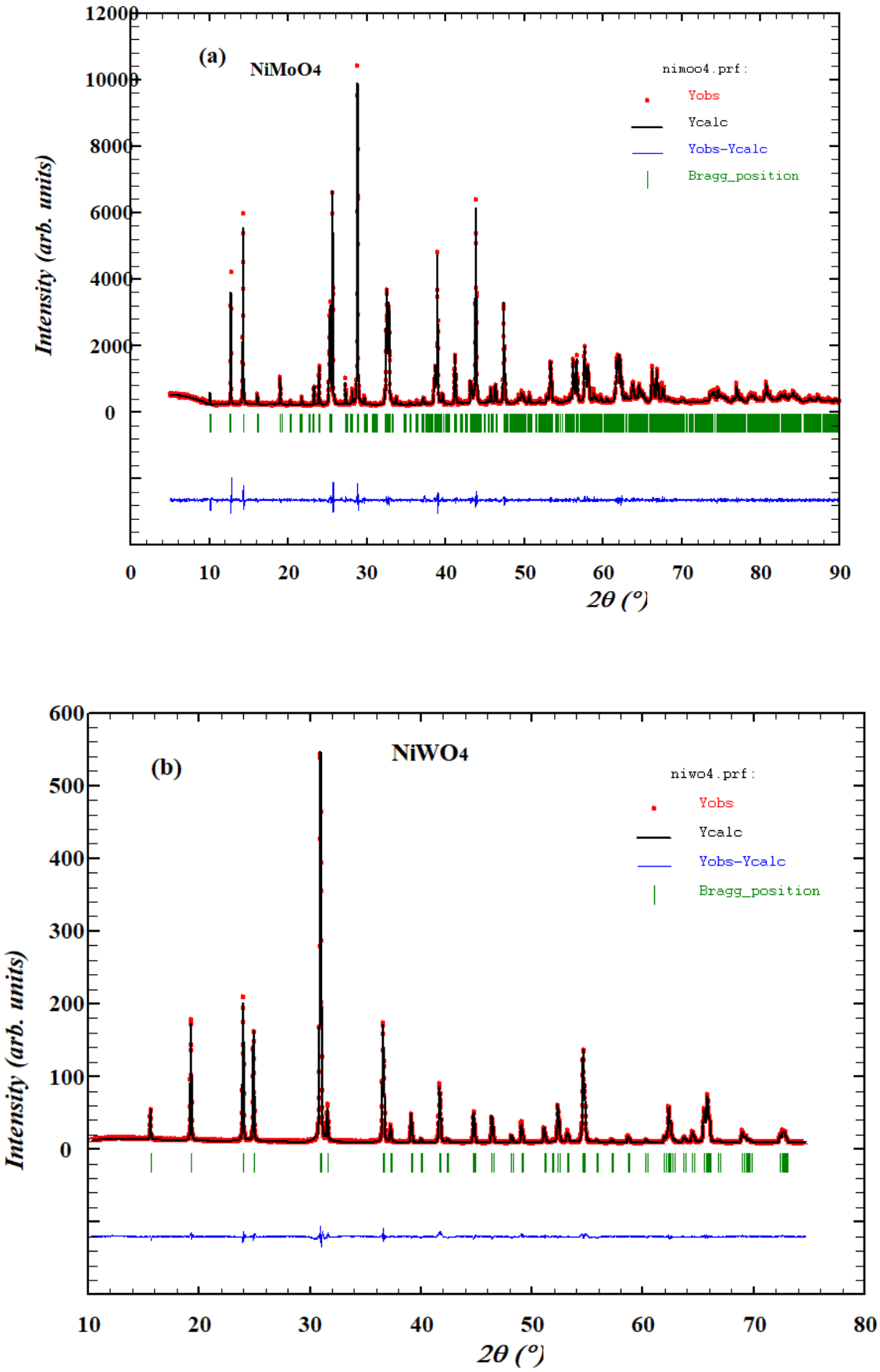
(a)
NiMoO4
nimoo4.prf:
Yobs
Ycalc
Yobs-Ycalc
Bragg_position
Intensity (arb. units)
2θ (°)
(b)
NiWO4
niwo4.prf:
Yobs
Ycalc
Yobs-Ycalc
Bragg_position
Intensity (arb. units)
2θ (°)

Fig.1 (a, b)

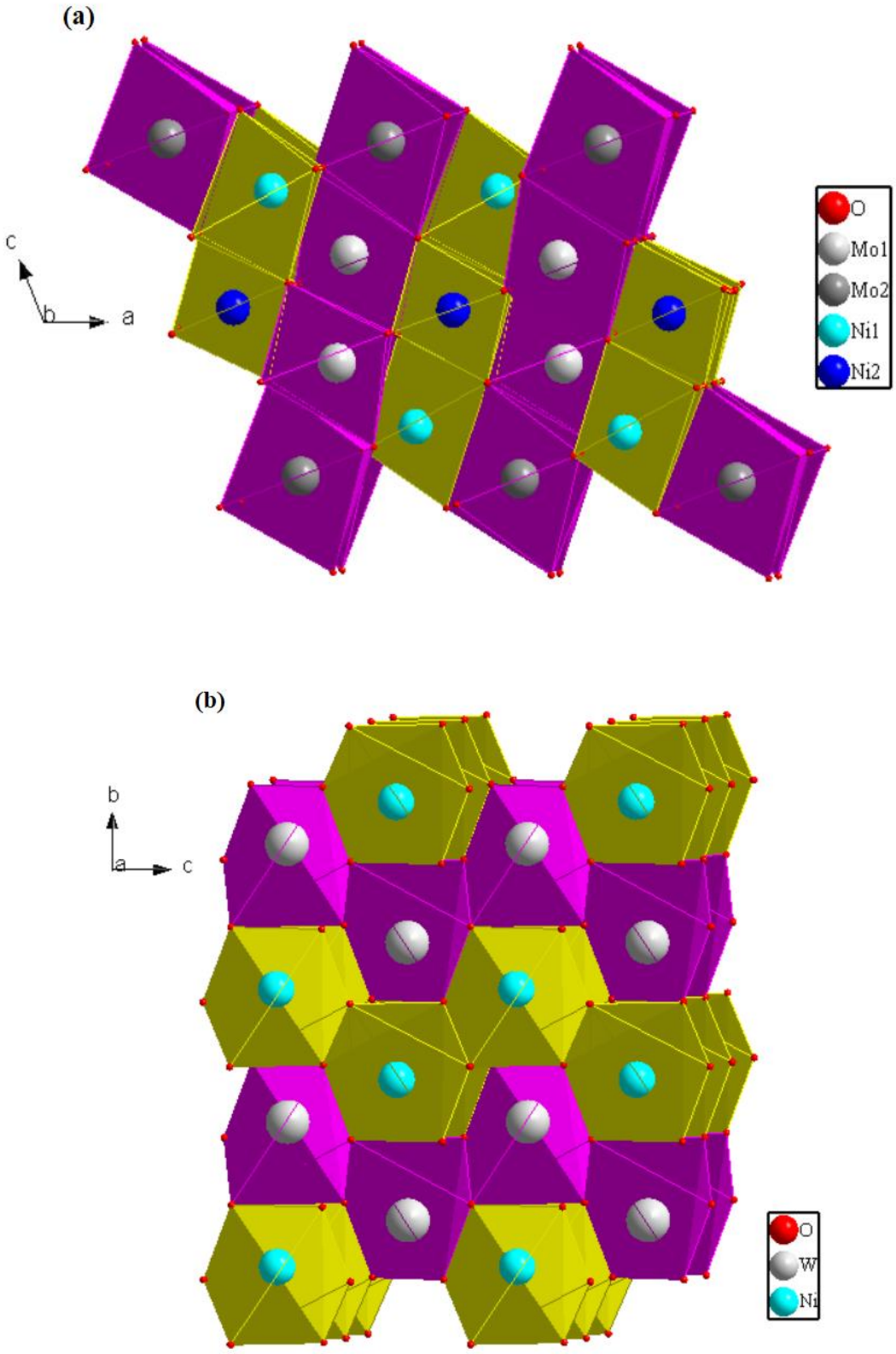

Fig 2. (a, b)

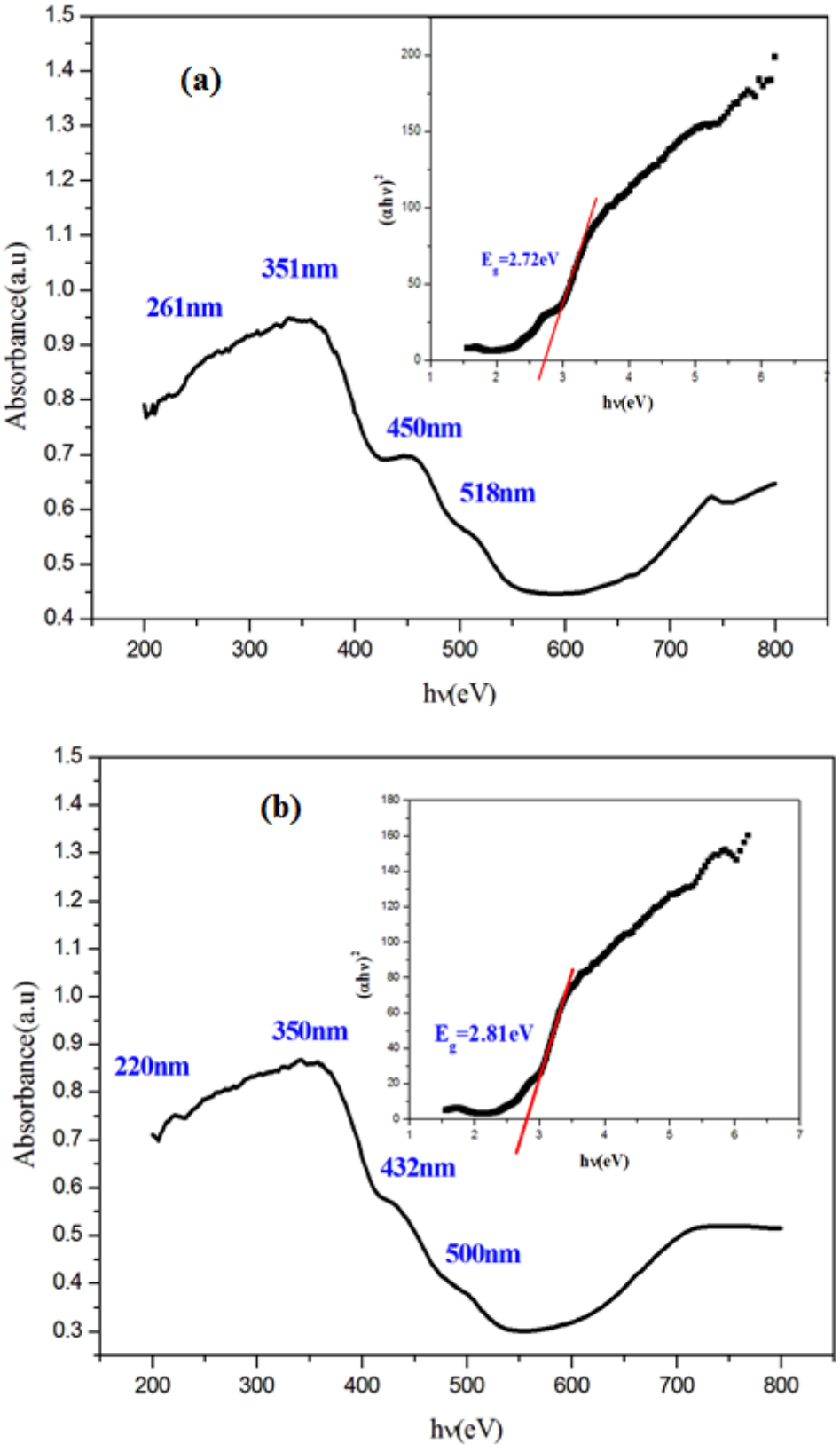
(a)
Absorbance(a.u)
hν(eV)
261nm
351nm
450nm
518nm
(αhν)²
E_g=2.72eV
hν(eV)
(b)
Absorbance(a.u)
hν(eV)
220nm
350nm
432nm
500nm
(αhν)²
E_g=2.81eV
hν(eV)

Fig. 3 (a, b)

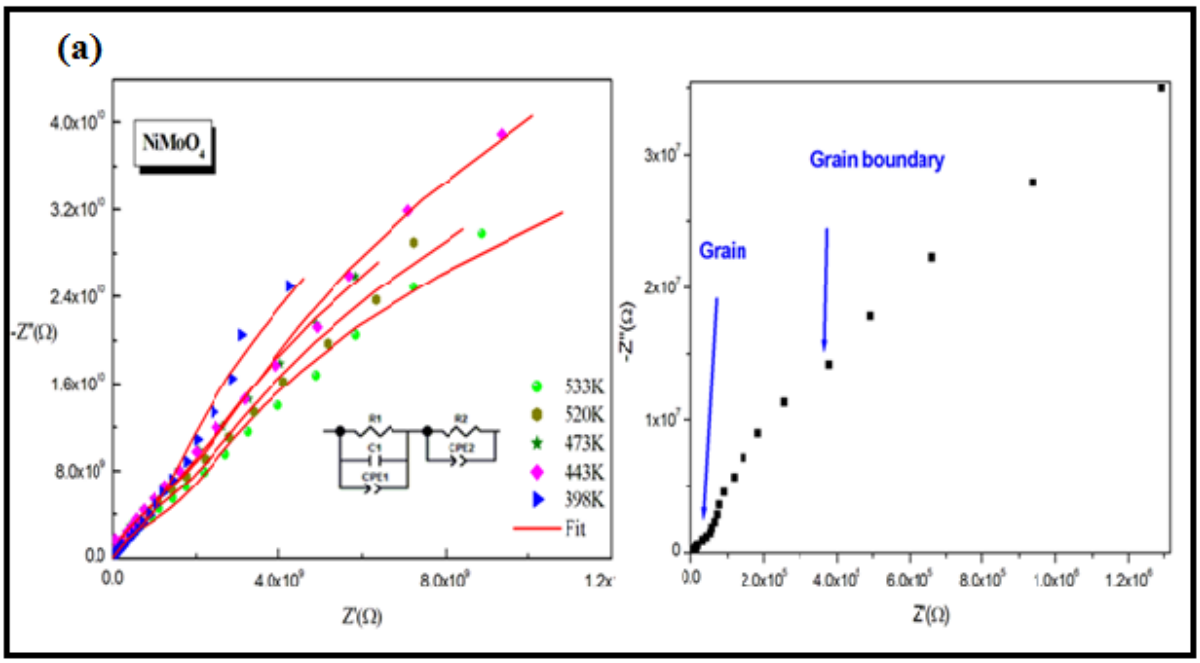
(a)
NiMoO4
-Z''(Ω)
Z'(Ω)
533K
520K
473K
443K
398K
Fit
R1
R2
C1
CPE1
CPE2
Grain boundary
Grain
-Z''(Ω)
Z'(Ω)

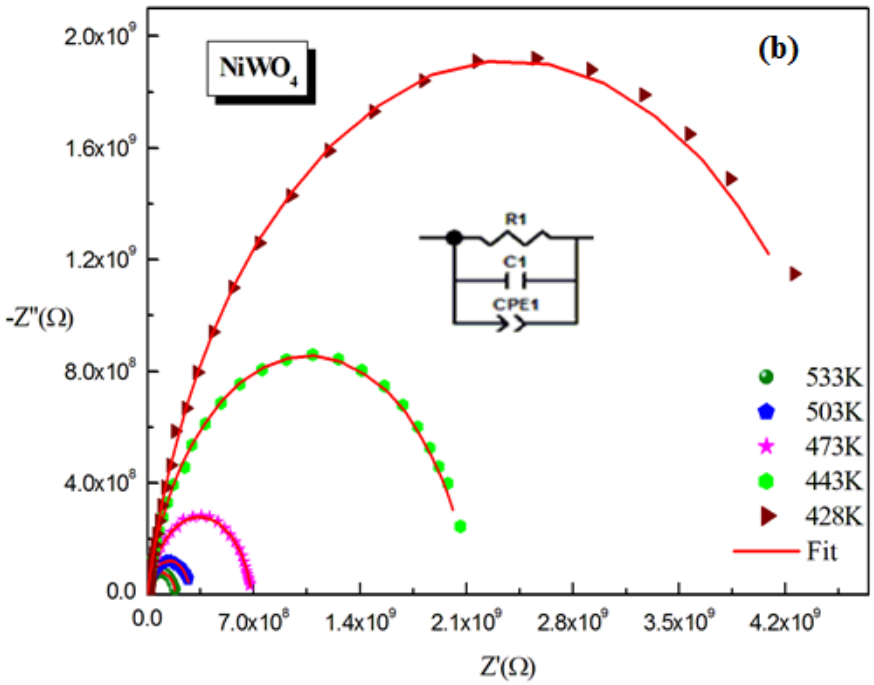
NiWO4
(b)
-Z''(Ω)
Z'(Ω)
R1
C1
CPE1
533K
503K
473K
443K
428K
Fit

Fig. 4 (a, b)

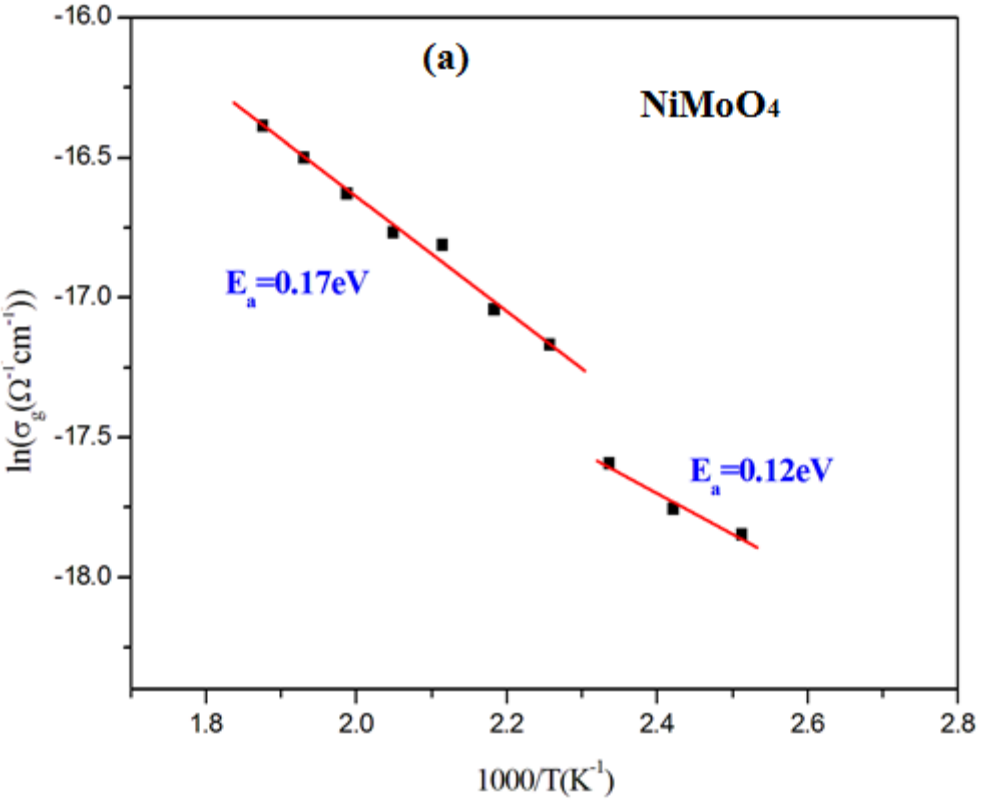
(a)
NiMoO4
Ea=0.17eV
Ea=0.12eV
ln(σg(Ω-1cm-1))
1000/T(K-1)
-16.0
-16.5
-17.0
-17.5
-18.0
1.8
2.0
2.2
2.4
2.6
2.8

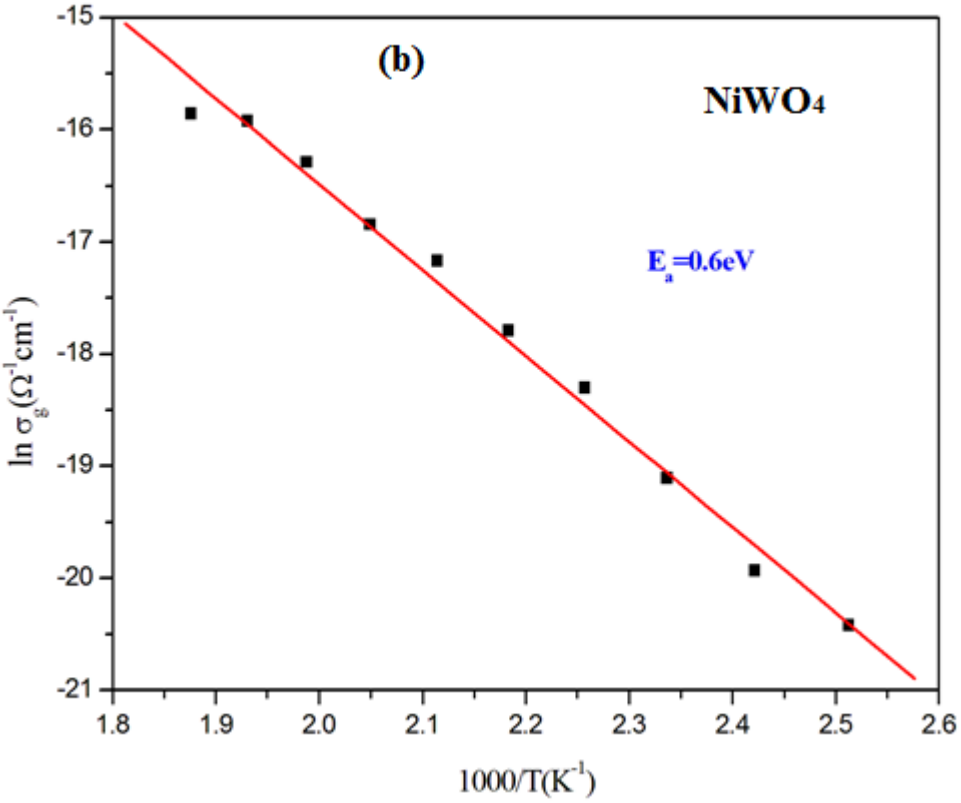
(b)
NiWO4
Ea=0.6eV
ln σg(Ω-1cm-1)
1000/T(K-1)
-15
-16
-17
-18
-19
-20
-21
1.8
1.9
2.0
2.1
2.2
2.3
2.4
2.5
2.6

Fig. 5 (a, b)

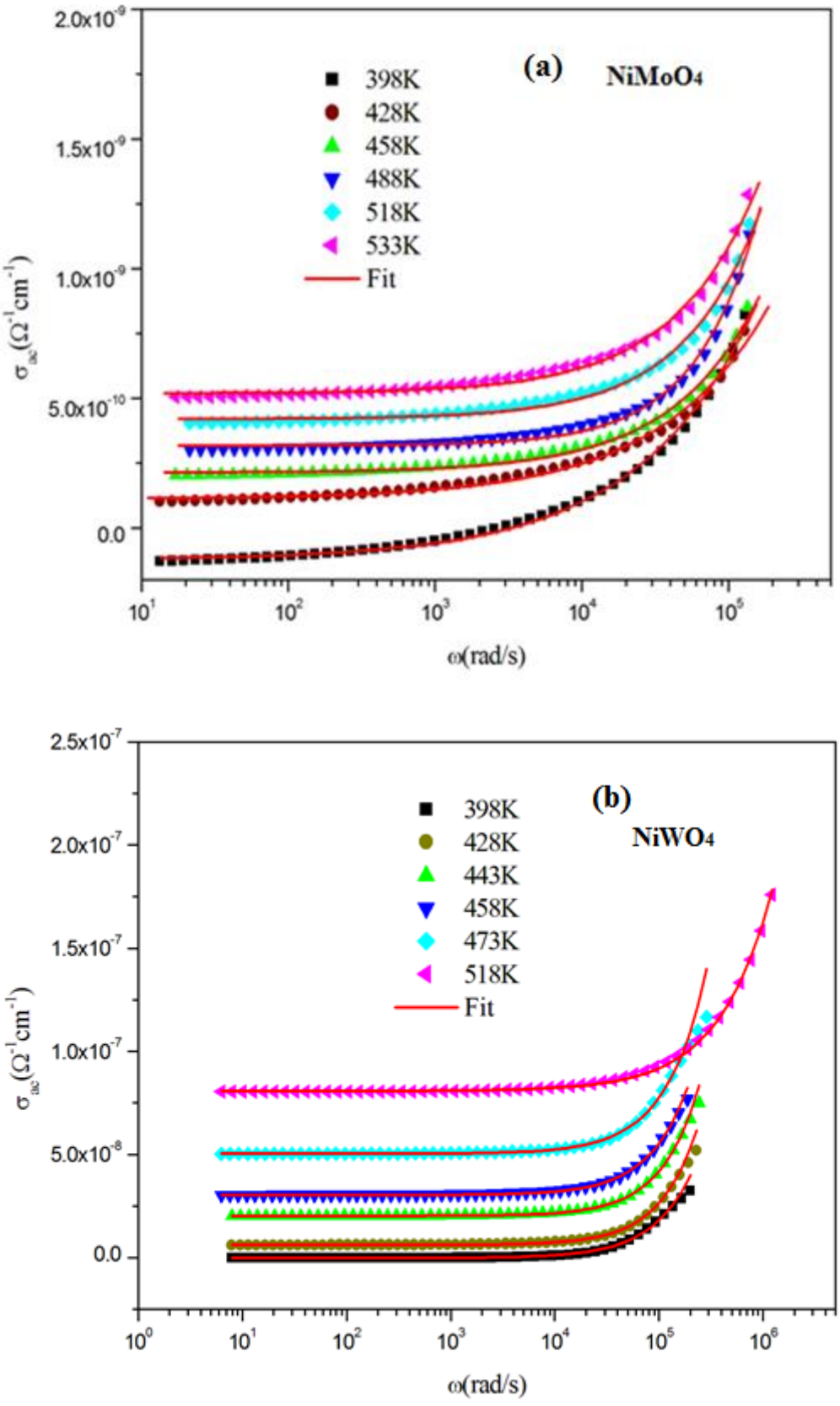
(a)
NiMoO4
398K
428K
458K
488K
518K
533K
Fit
2.0x10-9
1.5x10-9
1.0x10-9
5.0x10-10
0.0
σac(Ω-1cm-1)
10¹
10²
10³
10⁴
10⁵
ω(rad/s)
(b)
NiWO4
398K
428K
443K
458K
473K
518K
Fit
2.5x10-7
2.0x10-7
1.5x10-7
1.0x10-7
5.0x10-8
0.0
σac(Ω-1cm-1)
10⁰
10¹
10²
10³
10⁴
10⁵
10⁶
ω(rad/s)

Fig.6 (a, b)

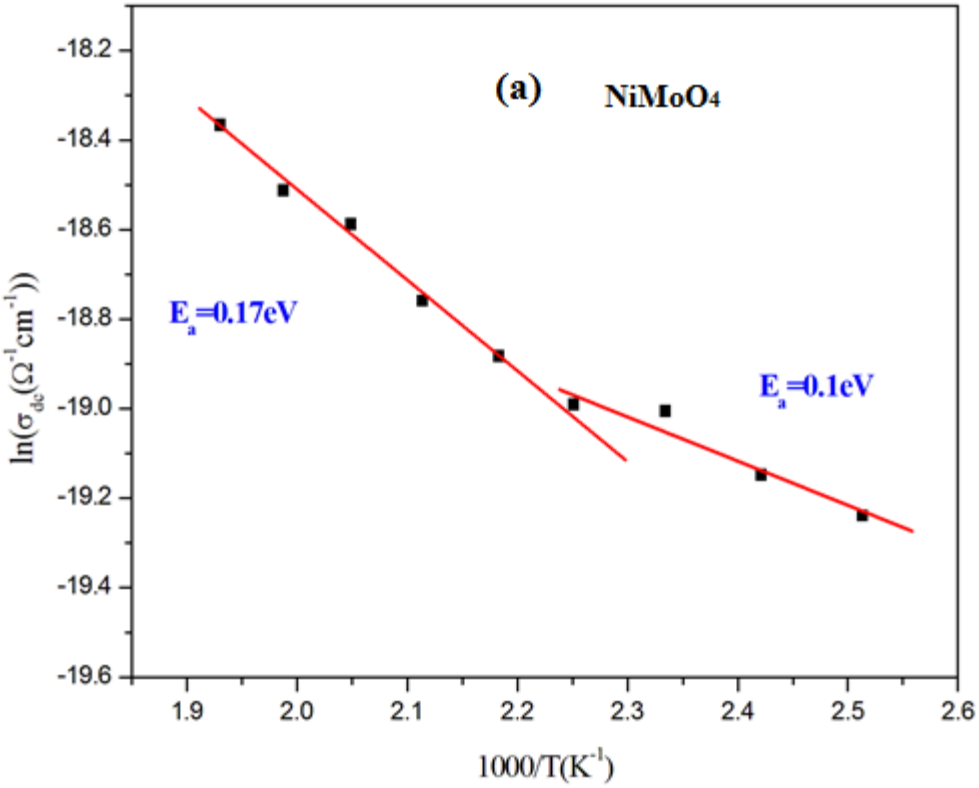
(a)
NiMoO4
Ea=0.17eV
Ea=0.1eV
ln(σdc(Ω-1cm-1))
1000/T(K-1)
-18.2
-18.4
-18.6
-18.8
-19.0
-19.2
-19.4
-19.6
1.9
2.0
2.1
2.2
2.3
2.4
2.5
2.6

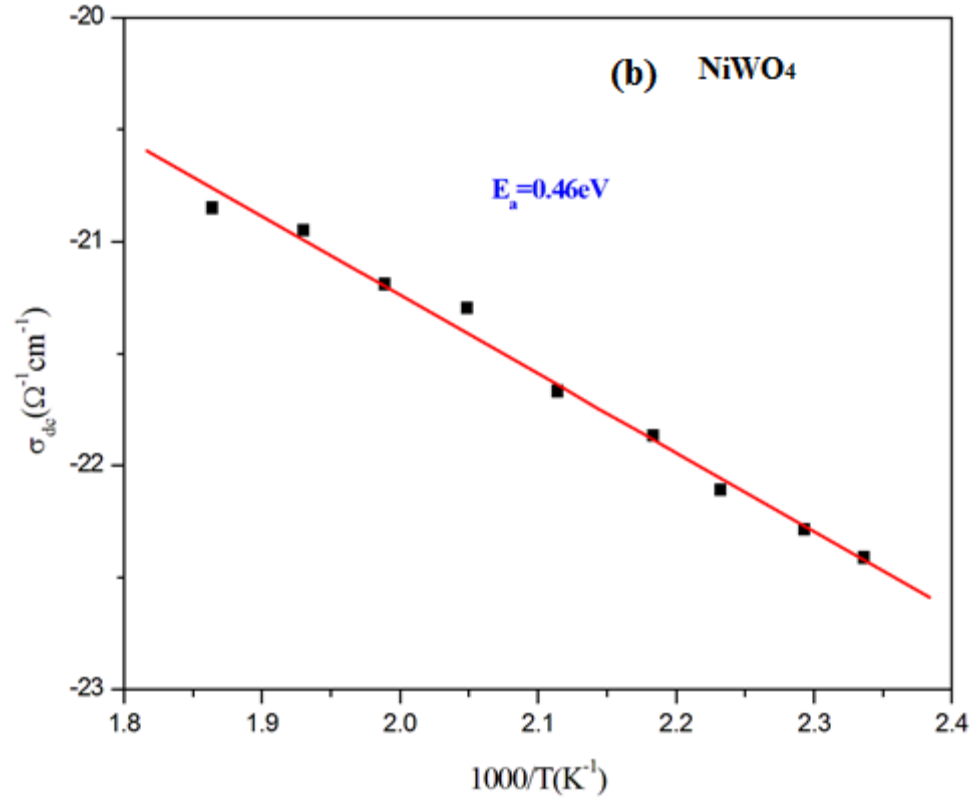
(b)
NiWO4
Ea=0.46eV
σdc(Ω-1cm-1)
1000/T(K-1)
-20
-21
-22
-23
1.8
1.9
2.0
2.1
2.2
2.3
2.4

Fig. 7 (a, b)

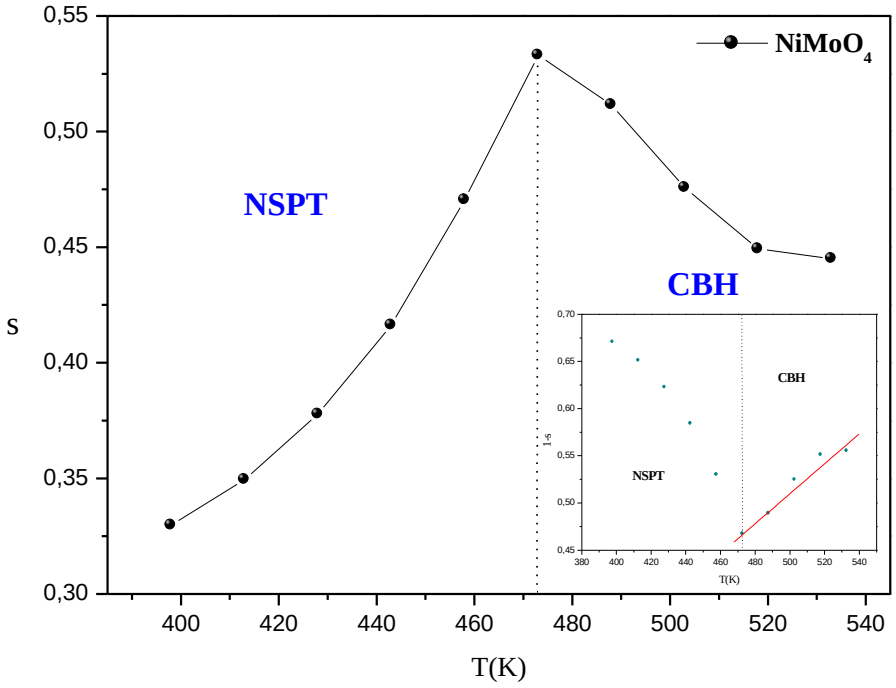
NiMoO4
NSPT
CBH
S
T(K)
0,55
0,50
0,45
0,40
0,35
0,30
400
420
440
460
480
500
520
540

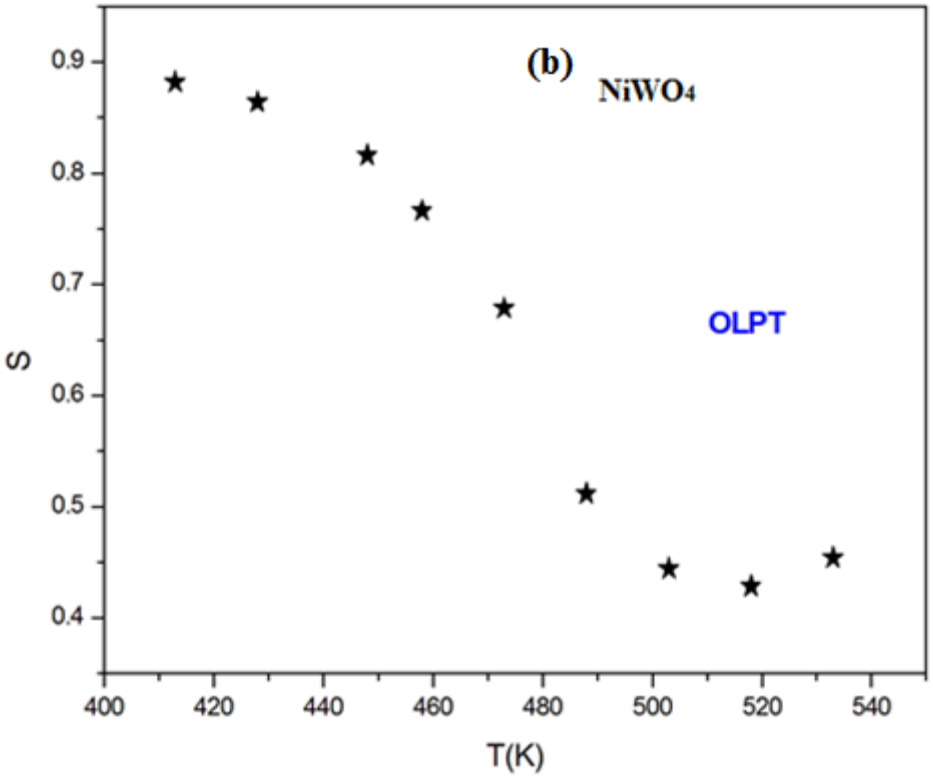
(b)
NiWO4
OLPT
S
T(K)
0.9
0.8
0.7
0.6
0.5
0.4
400
420
440
460
480
500
520
540

Fig. 8 (a, b)

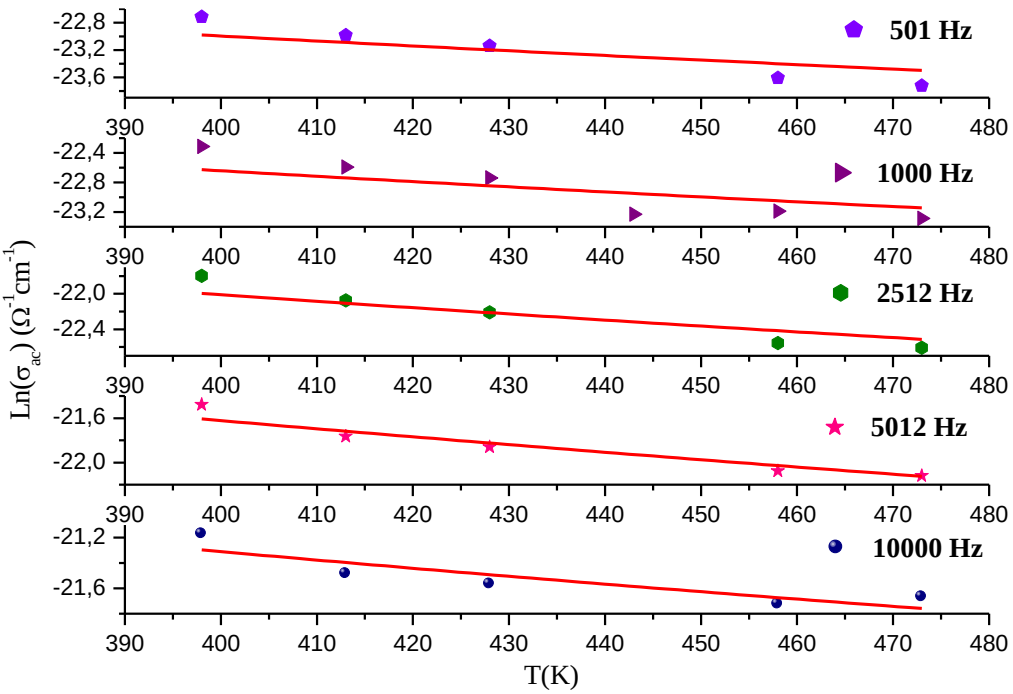
501 Hz
1000 Hz
2512 Hz
5012 Hz
10000 Hz
Ln(σ_ac) (Ω^-1 cm^-1)
T(K)

Fig. 9

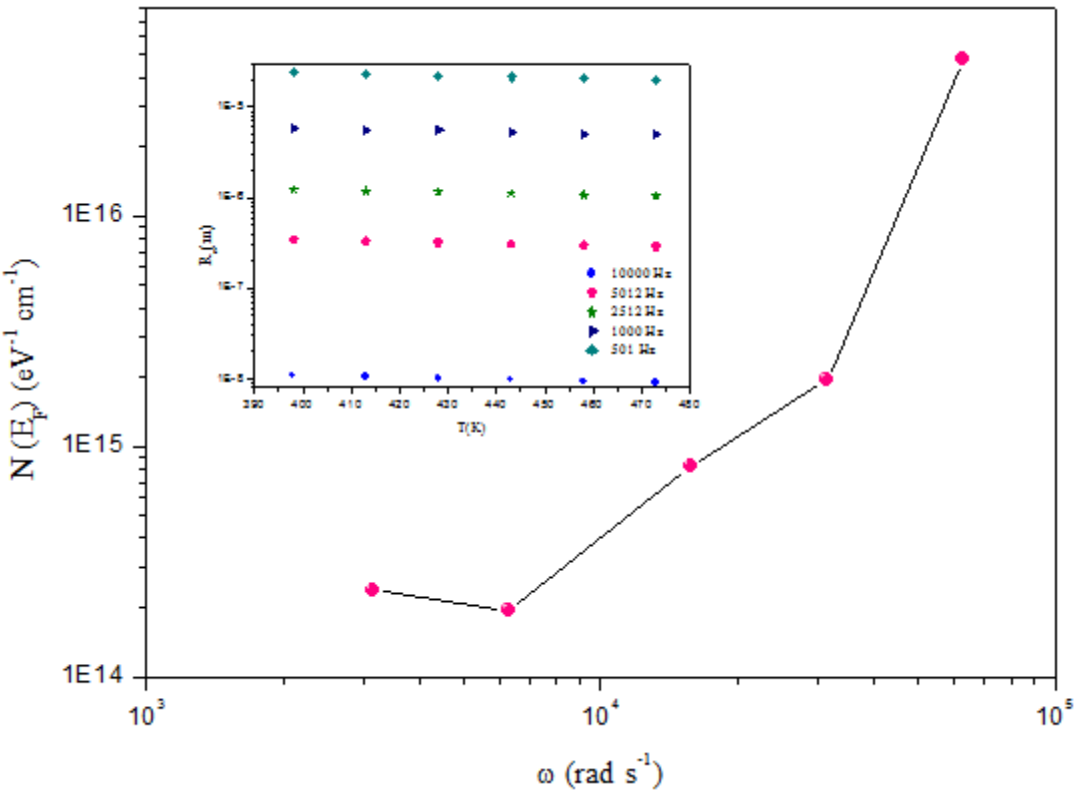
N (E_F) (eV^-1 cm^-1)
ω (rad s^-1)
1E16
1E15
1E14
10^3
10^4
10^5
R_g(Ω)
T(K)
10000 Hz
5012 Hz
2512 Hz
1000 Hz
501 Hz

Fig. 10

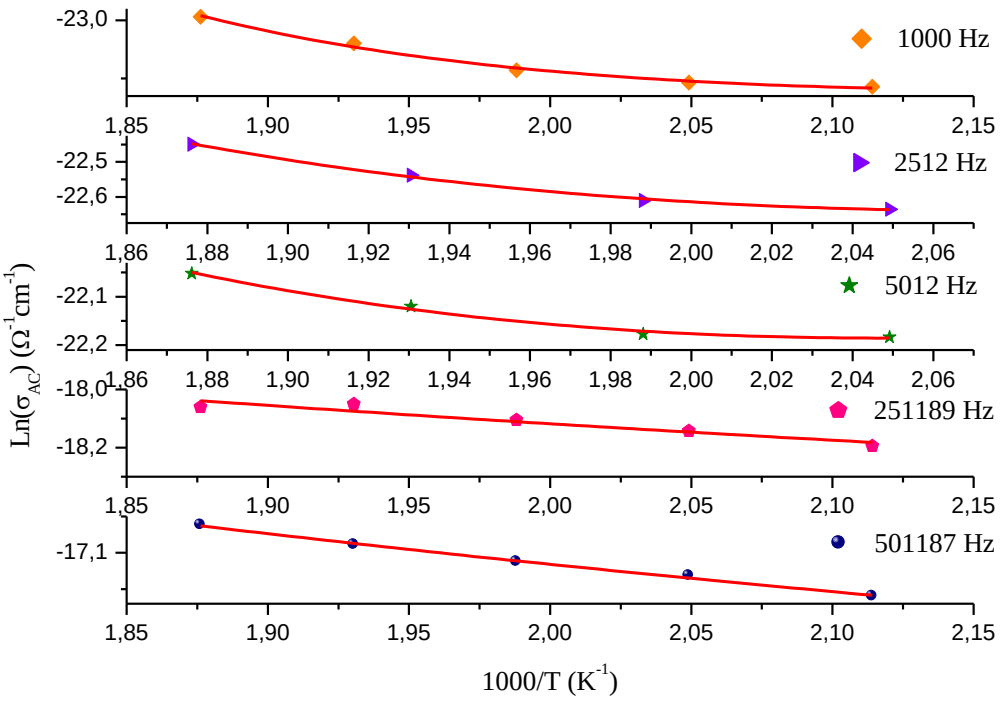
-23,0
1000 Hz
1,85
1,90
1,95
2,00
2,05
2,10
2,15
-22,5
-22,6
2512 Hz
1,86
1,88
1,90
1,92
1,94
1,96
1,98
2,00
2,02
2,04
2,06
-22,1
-22,2
5012 Hz
-18,0
-18,2
251189 Hz
-17,1
501187 Hz
Ln(σAC) (Ω-1cm-1)
1000/T (K-1)

Fig. 11

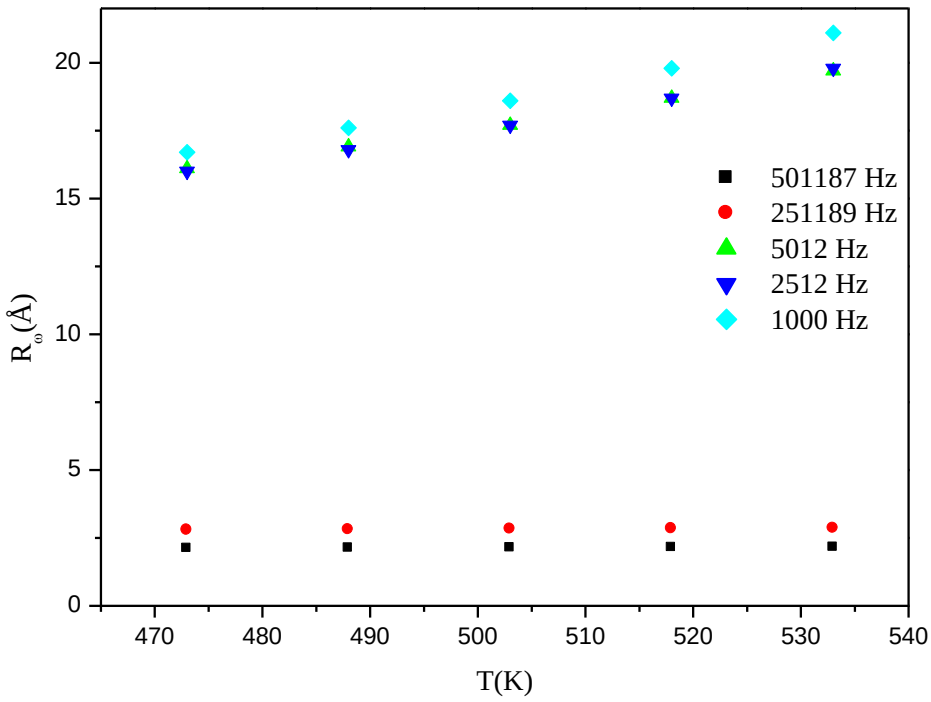
20
15
10
5
0
Rω (Å)
470
480
490
500
510
520
530
540
T(K)
501187 Hz
251189 Hz
5012 Hz
2512 Hz
1000 Hz

Fig. 12

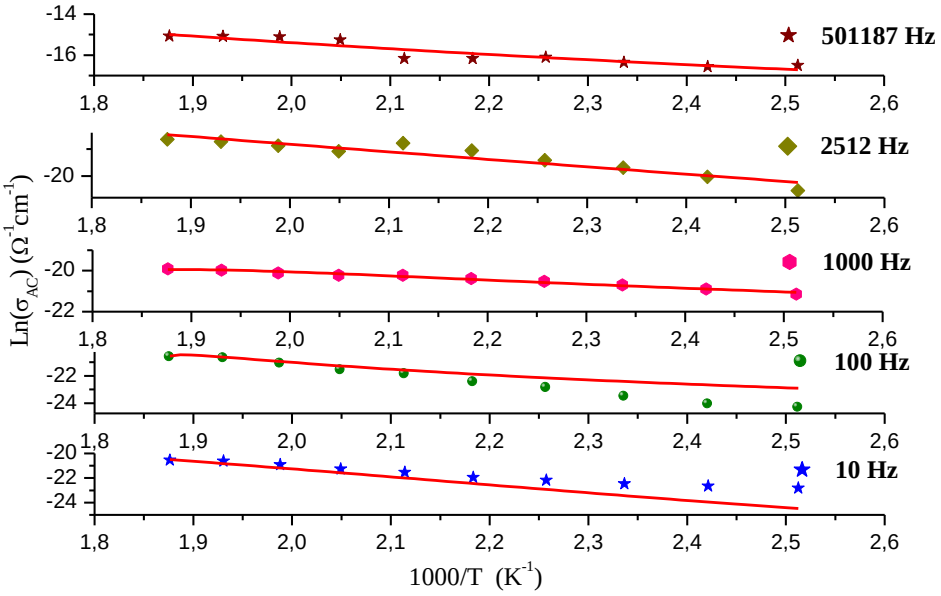
501187 Hz
2512 Hz
1000 Hz
100 Hz
10 Hz
Ln(σ_AC) (Ω^-1 cm^-1)
1000/T (K^-1)

Fig. 13

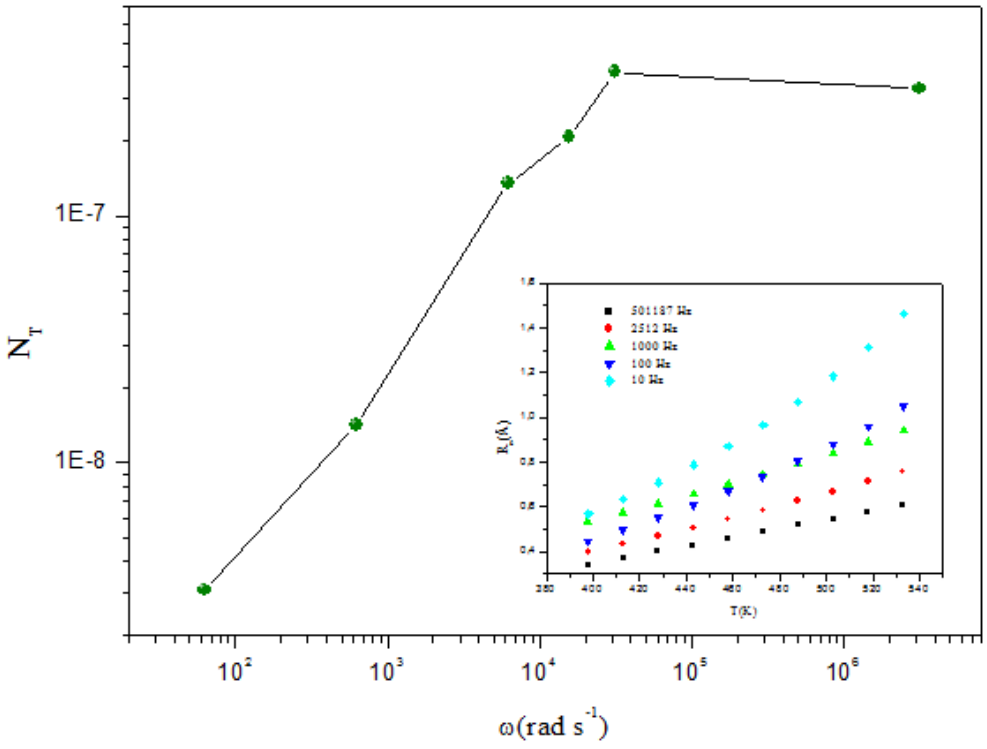
1E-7
1E-8
N_T
ω(rad s^-1)
501187 Hz
2512 Hz
1000 Hz
100 Hz
10 Hz
T(K)

Fig. 14

Table 1

	$NiMoO_4$	$NiWO_4$
Crystal system	monoclinic	monoclinic
Space group	C 2/m	P 2/c
a(Å)	9.5111	4.6013
b(Å)	8.7601	5.6632
c(Å)	7.6673	4.9103
β(°)	113.11	90.03
Volume V ($Å^3$)	587.56	127.95
Z	8	4
R_B factor (%)	**5.90**	**3.68**
R_F Factor (%)	**5.55**	**3.03**
X^2	**4.93**	**1.05**

Table 2

$NiMoO_4$					$NiWO_4$				
Atom	**Wyck.**	**x**	**y**	**Z**	**Atom**	**Wyck.**	**x**	**y**	**Z**
O1	8j	0.014	0.234	0.2855	**O1**	4g	0.223	0.113	0.924
O2	8j	0.166	0.2978	0.078	**O2**	4g	0.269	0.617	0.536
O3	8j	0.346	0.1370	0.434	**W1**	2f	0.5	0.677	0.25
O4	4i	0.205	0	0.093	**Ni1**	2e	0	0.163	0.25
O5	4i	0.158	0	0.579					
Mo1	4i	0.1976	0	0.3420					
Mo2	4g	0	0.2144	0					
Ni1	4i	0.7972	0	0.1474					
Ni2	4h	0	0.1916	0.5					

Table 3

	$NiMoO_4$	$NiWO_4$
Ni-O Polyhedral	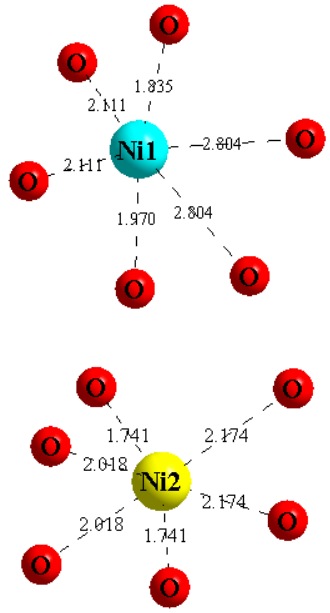	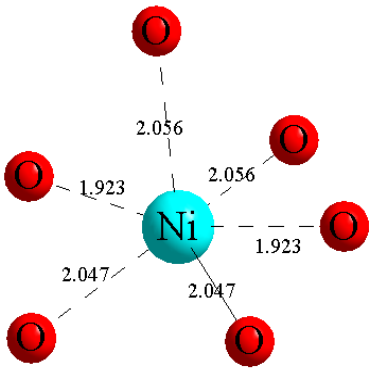
M-O polyhedral	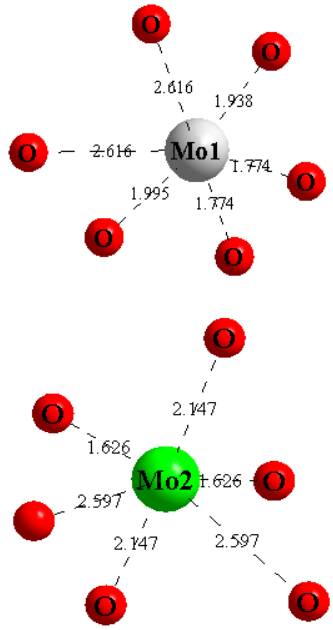	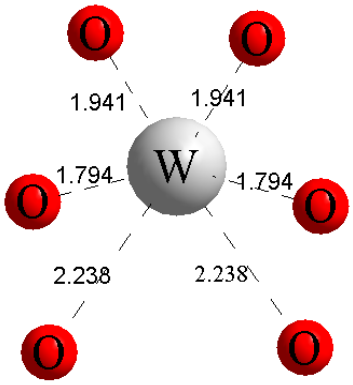

Table 4

Frequency(Hz)	$N(eV^{-1}m^{-1})$	$W_m(eV)$
501187	2.05×10^{16}	5.28
251189	3.15×10^{16}	4.07
5012	2.67×10^{17}	1.36
2512	3.88×10^{17}	1.39
1000	6.35×10^{17}	1.40

Table 5

Frequency (Hz)	$\alpha(Å^{-1})$	W_{H0} (eV)	$r_p(Å)$
10	1	1.20378	0.64413
100	1	1.20492	0.66692
1000	1	1.17775	0.83757
2512	1	1.16645	0.76453
501187	1	0.62774	0.6839